

# AN ENHANCED FINITE VOLUME BASED SOLVER FOR THERMOELASTIC MATERIALS IN FLUID-STRUCTURE COUPLED PROBLEMS

IGNACIO GONZÁLEZ, ALIREZA NASERI, JORGE CHIVA, JOAQUIM RIGOLA AND CARLOS D. PÉREZ-SEGARRA

Heat and Mass Transfer Technological Center (CTTC)  
Universitat Politècnica de Catalunya - BarcelonaTech (UPC)  
ESEIAAT, Colom 11, 08222 Terrassa (Barcelona), Spain  
e-mail: nacho@cttc.upc.edu, web page: <http://www.cttc.upc.edu/>

**Key words:** Thermoelasticity, Finite volume, Segregated method, Block-coupled method

**Abstract.** Enhanced finite volume thermoelastic models, with emphasis on convergence acceleration and direct face gradient calculation, are presented. Second-order discretisation schemes are employed in time and space, and two different approaches to solve the linear system of equations have been implemented: a segregated method and a block-coupled method. The accuracy and execution time requirements of the solvers are studied for three different cases, both with static and transient conditions. Significant savings in computation time are achieved owing to the acceleration strategies, without compromising the solution accuracy.

## 1 INTRODUCTION

Finite volume method has proved to be a reliable numerical approach to solve a great variety of computational structural mechanics phenomena. Early and current works on this topic can be found for example in [1–4]. In general, discretisation schemes are cell-centred, and the equations of each displacement direction are decoupled in three different linear systems. Thus, displacement inter-component dependencies are deferred to the source term and a fixed-point iterative process is needed. The final segregated model provides a simple and conservative formulation (in local and global momentum equilibrium), which employs very low memory usage but can experience slow convergence rates when there is strong coupling between displacement directions. This would be particularly disadvantageous in front of other structural solvers when considering partitioned implicit fluid-structure interaction cases, which requires solving both domains multiple times per time step.

Consequently, different solutions to accelerate the solution convergence have been proposed in the literature. A full multigrid algorithm based on V cycles and a correction scheme was used in [5]. In [6], the entire elasticity equation was arranged in a single linear system by integrating the discretisation coefficients of the displacement gradient into

a coupled matrix. The method was tested and applied to study structure-electrostatics interaction in microelectromechanical systems, showing dramatical improvement in the convergence rate. Similarly, [7] defined a block-coupled solver for linear elasticity which resulted in less execution time and memory requirements than a finite element software for the set of cases tested. Unlike [6], the displacement gradient was directly calculated on the faces, hence shrinking the gradient stencil of nodes and improving accuracy.

In this work, two different finite volume approaches for thermoelasticity problems in 3D unstructured meshes, with emphasis on convergence acceleration of the linear system resolution, are presented. The first one relates to a segregated method with Aitken acceleration and gradient-stress evaluation directly on the volume faces. The second is based on the block-coupled arrangement developed by [7]. First, the governing equations and the main highlights of the numerical implementation are described. Then, the models are validated and their computing performance analysed in static and transient cases.

These structural solvers are to be used within our semi-implicit partitioned fluid-structure interaction method, which has been already validated and applied for industrial applications [8–10]. In this manner, a common finite volume framework will be used for both domains, ensuring a consistent coupling strategy and a conservative resolution of the governing equations.

## 2 GOVERNING EQUATIONS

The lagrangian form of the linear momentum equation integrated over a control volume  $V$ , bounded by the surface  $S$ , can be written as:

$$\int_V \frac{\partial^2 (\rho \mathbf{u})}{\partial t^2} dV = \int_S \mathbf{n} \cdot \boldsymbol{\sigma} dS, \quad (1)$$

where  $\rho$  is the density,  $\mathbf{u}$  the displacement,  $\mathbf{n}$  the surface unit normal vector pointing outwards, and  $\boldsymbol{\sigma}$  is the Cauchy stress tensor.

Hooke's law for isotropic linear thermoelastic materials relates the stresses with displacements and temperatures:

$$\boldsymbol{\sigma} = \mu \nabla \mathbf{u} + \mu (\nabla \mathbf{u})^T + \lambda \text{tr}(\nabla \mathbf{u}) \mathbf{I} - \beta (T - T_0) \mathbf{I}, \quad (2)$$

where  $\lambda$  and  $\mu$  are the first and second Lamé's parameters, respectively. The parameter  $\beta$  is related to the coefficient of linear thermal expansion  $\alpha$  by

$$\beta = \alpha (2\mu + 3\lambda). \quad (3)$$

In this manner, the first stress term of Eq. 1 ( $\mu \mathbf{n} \cdot \nabla \mathbf{u}$ ) behaves as a diffusion term and its discretisation is straightforward, as will be shown later. Taking into account the optimal implicit contribution for the segregated method [2], both the laplacian transpose term and the laplacian trace of the displacement will be treated as a normal laplacian, and a deferred correction will assign the correct values of the total stress. Therefore, the arrangement of the segregated model for Eq. 1 reads:

$$\int_V \frac{\partial^2 (\rho \mathbf{u})}{\partial t^2} dV - \int_S (2\mu + \lambda) \mathbf{n} \cdot \nabla \mathbf{u} dS = \int_S \mathbf{n} \cdot (\boldsymbol{\sigma} - (2\mu + \lambda) \nabla \mathbf{u}) dS, \quad (4)$$

where right-hand side will be allocated to the source term.

On the other hand, the block-coupled approach treats the entire stress term implicitly, considering separately the surface normal and tangential derivatives in the following fashion [7]:

$$\int_V \frac{\partial^2 (\rho \mathbf{u})}{\partial t^2} dV - \int_S ((2\mu + \lambda) \mathbf{n} \cdot \nabla \mathbf{u}_n + \lambda \mathbf{n} \text{tr} (\nabla_t \mathbf{u}_t) + \mu \mathbf{n} \cdot \nabla \mathbf{u}_t + \mu \nabla_t u_n) dS = - \int_S \mathbf{n} \beta (T - T_0) dS, \quad (5)$$

where  $\mathbf{u}_n = \mathbf{n} \mathbf{n} \cdot \mathbf{u}$ ,  $\mathbf{u}_t = (\mathbf{I} - \mathbf{n} \mathbf{n}) \cdot \mathbf{u}$ ,  $u_n = \mathbf{n} \cdot \mathbf{u}$ , and tensor  $\mathbf{n} \mathbf{n}$  results from the dyadic product of normal vector. The surface tangential derivatives of any variable  $\phi$  are equivalent to  $\nabla_t \phi = (\mathbf{I} - \mathbf{n} \mathbf{n}) \cdot \nabla \phi$ .

The temperature distribution  $T$  is governed by the energy conservation equation. Considering quasi-static linear thermoelastic problems, temperature becomes independent of the strain rate, and energy balance reduces to a conduction heat transfer equation [11].

### 3 NUMERICAL METHOD

The domain is divided into arbitrary convex polyhedral cells, where the conservation equations are integrated. The system of equations is written as a function of the value of the displacements in cell centres and boundary face centres (all treated as nodes). Since the stress term of Eq. 1 is integrated over the cell faces, here both gradient and stress are discretised directly on the faces, instead of interpolating their value from the adjacent cell centres.

#### 3.1 Temporal discretization

The momentum equation is solved using a direct implicit time integration, where all terms are evaluated from the state of the system at the current instant. The inertial term is formulated according to the trapezoidal rule, which is second-order accurate, unconditionally stable for linear analysis and shows limited integration errors [12, 13]. The resulting equations for the velocity  $\dot{\mathbf{u}}$  and displacement at the current time are

$$\dot{\mathbf{u}}^{n+1} = \dot{\mathbf{u}}^n + \frac{\ddot{\mathbf{u}}^{n+1} + \ddot{\mathbf{u}}^n}{2} \Delta t, \quad (6)$$

$$\mathbf{u}^{n+1} = \mathbf{u}^n + \dot{\mathbf{u}}^n \Delta t + \frac{\ddot{\mathbf{u}}^{n+1} + \ddot{\mathbf{u}}^n}{4} \Delta t^2. \quad (7)$$

The acceleration  $\ddot{\mathbf{u}}^{n+1}$  can be expressed in terms of  $\mathbf{u}^{n+1}$  from Eq. 7, and thus be used within the inertial term of the equilibrium equation,  $\partial^2 (\rho \mathbf{u}) / \partial t^2$ . Following the linear formulation for small strains,  $\rho$  is assumed constant over time.

#### 3.2 Gradient discretization

Like in the block-coupled solver of [7], the gradient is calculated directly on the face by numerical schemes which compute normal and tangential components of the gradient

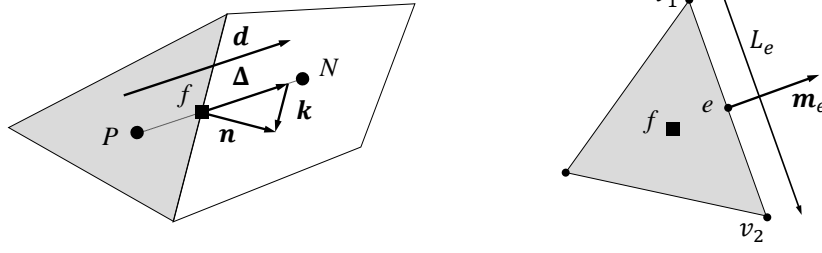


**Figure 1:** Geometrical relations between two adjacent cells (left) and face-edge parameters (right).

separately,

$$(\nabla\phi)_f = (\nabla_n\phi)_f + (\nabla_t\phi)_f, \quad (8)$$

where  $\phi$  can be any scalar or vector field stored in the nodes.

In this work this normal-tangential gradient decomposition is extended to the segregated method too, in order to obtain an equivalent discretisation with both methods and just a different manner to deal with the resulting linear system of equations in each one.

The face normal derivative includes an orthogonal contribution and a non-orthogonal correction:

$$(\nabla_n\phi)_f = \mathbf{n}_f (\mathbf{n} \cdot \nabla\phi)_f \approx \mathbf{n}_f \left( |\mathbf{\Delta}| \frac{\phi_N - \phi_P}{|\mathbf{d}|} + (\mathbf{k} \cdot \nabla_t\phi)_f \right), \quad (9)$$

where  $\mathbf{d} = \mathbf{x}_N - \mathbf{x}_P$ ,  $\mathbf{\Delta} = \mathbf{d} / (\mathbf{d} \cdot \mathbf{n})$  and  $\mathbf{k} = \mathbf{n} - \mathbf{\Delta}$ , as can be seen in Fig. 1. The selected vector  $\mathbf{k}$  is tangent to the face  $f$ , allowing for evaluating the non-orthogonal correction with  $(\nabla_t\phi)_f$  instead of with the total face gradient.

To calculate the face tangential derivative, the surface Gauss theorem is employed [14], which integrates along the face edges  $e$  as follows:

$$(\nabla_t\phi)_f \approx \frac{1}{S} \sum_e \mathbf{m}_e L_e \phi_e, \quad (10)$$

where  $L_e$  is the length of the straight edge and  $\mathbf{m}_e$  is the unit vector parallel to the face and perpendicular to the edge (see Fig. 1). The edge value  $\phi_e$  is obtained by averaging the value of  $\phi$  in the edge vertices  $v_1$  and  $v_2$ . Therefore, a vertex interpolation procedure, to interpolate the node-centred displacement to the grid vertices, is needed. For this purpose, in lieu of a Least Squares interpolation with linear fit function, the modified Shepard interpolation described by [15], which is exact for linear polynomials, is used. The former should solve a  $4 \times 4$  system for each vertex, whereas the latter deals with a  $3 \times 3$  system, hence greatly decreasing the computational effort. The final value of the field in the vertex results in a linear combination of its value in the surrounding nodes, indexed as  $vn$ ,

$$\phi_v = \sum_{vn} \omega_{vn} \phi_{vn}. \quad (11)$$

Finally, the tangential derivative discretisation of Eq. 10 relative to the node values becomes

$$(\nabla_t \phi)_f \approx \frac{1}{S} \sum_e \left( \mathbf{m}_e L_e \sum_{vn} \frac{1}{2} \omega_{vn} \phi_{vn} \right). \quad (12)$$

In the segregated method, the orthogonal contribution of Eq. 9 is used to discretise implicitly the diffusion term of Eq. 4. The face gradient and face stress are computed via Eqs. 9, 12 and 2 with the last value of the displacement, and added to the system source term. In the block-coupled method, the whole derivative discretisation is considered implicitly. For more information about the block-coupled methodology, the reader is referred to [7].

### 3.3 Boundary conditions

Three types of boundary conditions have been implemented:

- Known displacement (Dirichlet):  $\mathbf{u}_B = \mathbf{U}$ .
- Zero normal gradient of the displacement (Neumann):  $(\mathbf{n} \cdot \nabla \mathbf{u})_B = \mathbf{0}$ . Following the numerical scheme for the normal derivative (Eq. 9), the resulting expression of the boundary node is

$$|\Delta| \frac{\mathbf{u}_B - \mathbf{u}_N}{|\mathbf{d}|} + (\mathbf{k} \cdot \nabla_t \mathbf{u})_B = \mathbf{0}, \quad (13)$$

where the non-orthogonal correction is evaluated with Eq. 12. In the segregated method, this correction is added to the source term, whereas in the block-coupled method it is considered implicitly.

- Known external traction:  $(\mathbf{n} \cdot \boldsymbol{\sigma})_B = \mathbf{T}$ . The discretisation of this boundary condition is the same as the one employed to discretise the internal face stress.

A symmetry plane is represented as a Dirichlet condition in the normal component of the displacement and a Neumann condition in the tangential directions.

### 3.4 Linear system resolution

As already mentioned, the segregated method moves the inter-component dependencies of the thermoelasticity equation to the source term. Consequently, three linear symmetric systems, one for each direction, are defined. The implicit momentum equilibrium should be solved then performing fixed-point iterations, where the source is updated after every iteration. To accelerate the solution convergence, a multidimensional Aitken  $\Delta^2$  technique [16] is proposed:

$$\tilde{\mathbf{u}}^{k+2} = \mathbf{u}^{k+2} + \gamma \mathbf{r}^{k+2}, \quad (14)$$

$$\gamma = \frac{\mathbf{r}^{k+2} \cdot (\mathbf{r}^{k+2} - \mathbf{r}^{k+1})}{|\mathbf{r}^{k+2} - \mathbf{r}^{k+1}|^2}, \quad (15)$$

$$\mathbf{r}^{k+2} = \mathbf{u}^{k+2} - \mathbf{u}^{k+1}. \quad (16)$$

It has been found that applying this Aitken formula every five iterations provides an optimum convergence acceleration for the particular cases analysed in this work.

Thus, each time step is solved by an iterative process, where every iteration performs the next tasks: solve all three linear systems  $[A_i] \cdot \{u_i\} = \{B_i\}$ , relax the solution  $\{u_i\}$ , calculate  $(\nabla \mathbf{u})_f$  and  $\boldsymbol{\sigma}_f$ , update the source terms  $\{B_i\}$ , evaluate the maximum system initial residual  $|[A_i] \cdot \{u_i\} - \{B_i\}| / |\{B_i\}|$  and check for problem convergence if it is lower than  $10^{-7}$ . Since the source term does not provide the converged values from the beginning, there is no need to reach very tight tolerance in every linear system resolution.

On the other side, the block-coupled model joins all displacement dependencies into a single linear system. This generates a non-symmetric system with three times the size of the segregated systems. Furthermore, the matrix is less diagonally dominant and less sparse. The linear system is clearly harder to solve, considering numerical stability and memory requirements. However, as will be shown, the resulting convergence speed is notably higher than that obtained with the segregated methods.

Both methodologies employ parallel PETSc solvers [17,18]. A conjugate-gradient solver with  $10^{-2}$  error tolerance relative to the initial residual has been selected for all the segregated simulations, while a biconjugate gradient stabilized solver with  $10^{-7}$  relative error tolerance has been selected for the block-coupled ones.

## 4 RESULTS

In this section, the accuracy of numerical schemes is studied for three different cases, in static and transient conditions. Besides, the effectiveness to reduce the computational times of the segregated convergence acceleration and the block-coupled arrangement is analysed.

### 4.1 Case A: Thermal loading

NAFEMS Standard Benchmark Test LE11 [19] is solved to check the order of accuracy of the described formulation. A body of revolution with Young's modulus  $E = 210$  GPa, Poisson's ratio  $\nu = 0.3$  and thermal expansion coefficient  $\alpha = 2.3 \cdot 10^{-4} \text{ K}^{-1}$ , is subjected to static non-linear thermal loading, and thereby to thermal expansion and thermal stresses. Geometry, temperature rise function and boundary conditions can be found in Fig. 2. The target solution refers to  $\sigma_{zz}$  at point A, whose value should be  $-105$  MPa.

Due to the axisymmetric configuration, only a quarter of the cylindrical solid is modelled. Four different mesh refinements have been tested, each mesh doubling the number of divisions in all directions of the previous one. Thus, observing the second level of refinement shown in Fig. 2, the resulting number of cells of the meshes are: 60 (1), 480 (2), 3840 (3) and 30720 (4).

The relative error in stress in the specified point is plotted as a function of mesh size in Fig. 2. As can be seen, a second-order rate of convergence in the stress solution is obtained. Despite considering a point located in the domain boundary vertex, second-order accuracy can be achieved owing to the vertex interpolation technique and the second-order tangential derivative discretisation on inner and boundary faces. Although segregated and

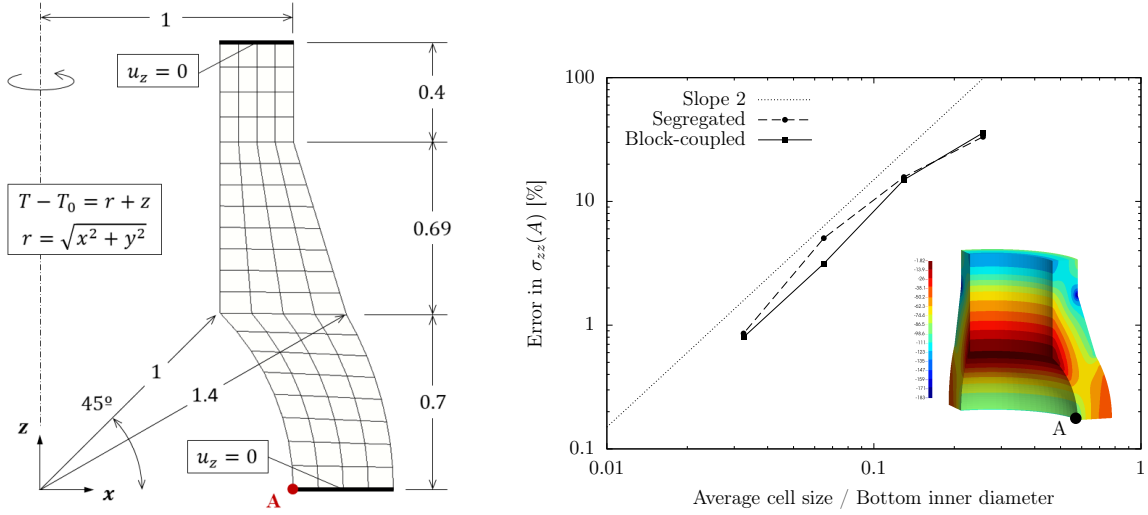


**Figure 2:** Case A: Problem description with Mesh 2 (left) and variation of relative error in  $\sigma_{zz}$  at point A (right). All boundary conditions not specified are traction free. Mesh 2 has 6 divisions in the azimuthal direction. Units in m, °C.

block-coupled methodologies share the same numerical schemes, minor discrepancies in this point stress arise with Mesh 3, probably due to convergence criteria or linear solvers operation.

The execution times consumed to run this case are presented in Table 1. In general, the computing demand of this case is very low for all meshes. The convergence acceleration introduced in the segregated approach is able to decrease the computing time with all mesh refinements, although the major savings in this sense are produced by the block-coupled method, which solves the problem up to 2.4 times faster than the proposed segregated method.

## 4.2 Case B: Bending of a thick plate

A thick elliptic plate under normal pressure, which suffers from static out-of-plate bending, was reproduced by [5] as a benchmark structural problem. Details of the domain and boundary conditions are depicted in Fig. 3. The material properties are  $E = 210$  GPa and  $\nu = 0.3$ . A quarter of the domain is again sufficient due to the double symmetry of the configuration. As in Case A, four systematically refined meshes have been tested: 72 (1), 576 (2), 4608 (3) and 36864 (4).

The distribution of  $\sigma_{xx}$  and  $\sigma_{yy}$  on the plate mid-section compared with the benchmark solution by [5] is delineated in Fig. 3. Like in the original solution, the symmetry between both stresses which would be expected with circumferential edges is disrupted by the elliptic shapes. The obtained solution agrees well with the benchmark, although visible differences can still be seen close to the symmetry boundaries, as a result of the mesh refinement. Convergence to the reference solution is distinctly proved observing Fig. 4, where  $x$  displacement and von Mises equivalent stress along line  $x = y$  on the plate mid-section are depicted and compared with results from [5].

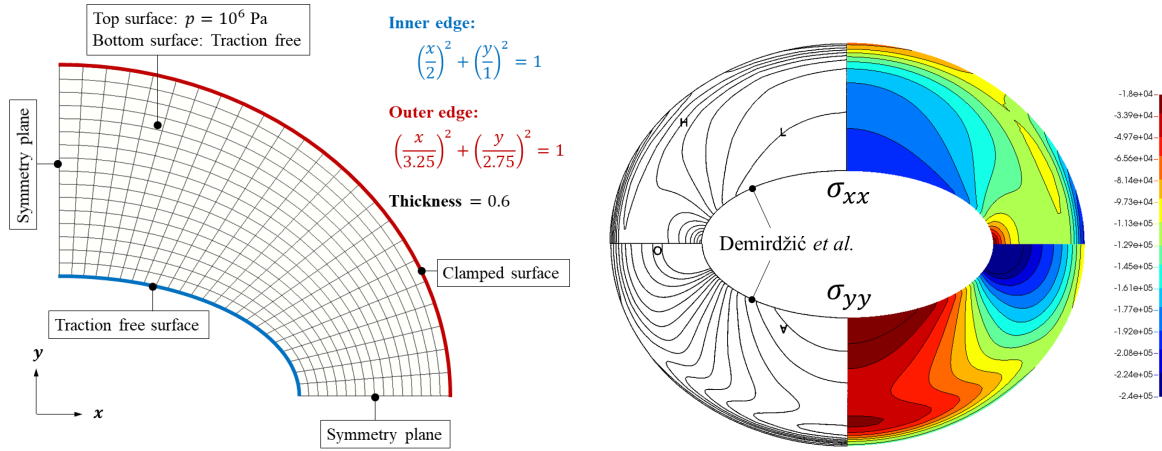


**Figure 3:** Case B: Problem description with Mesh 3 (left) and distribution of stress components on the plate mid-section obtained with Mesh 4 compared with results from [5] (right). Mesh 3 has 12 divisions in thickness. Units in m, Pa.

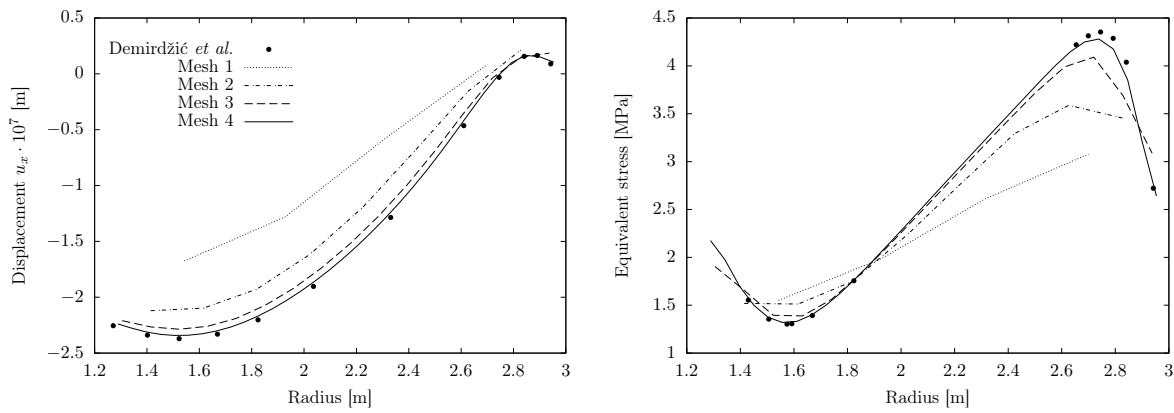


**Figure 4:** Case B: Distribution of  $u_x$  (left) and equivalent stress (right) on the plate mid-section along  $x = y$  compared with results from [5].

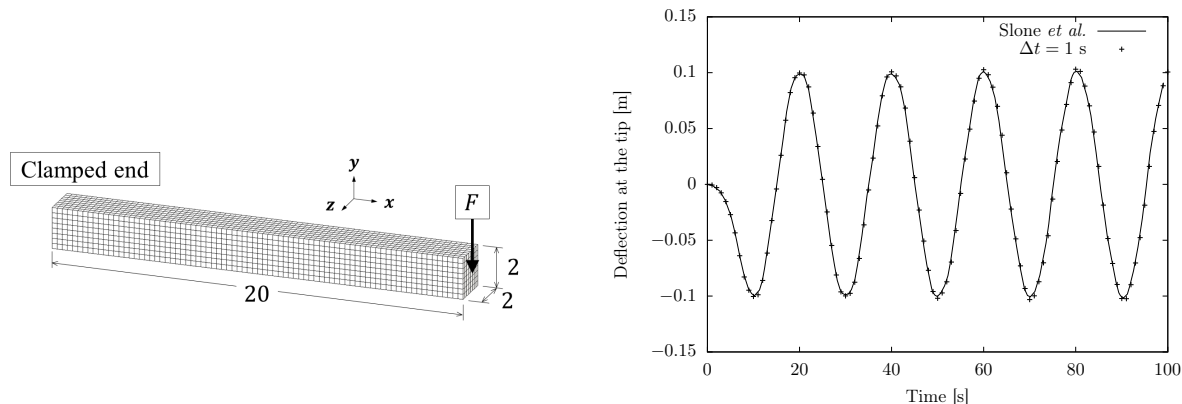


**Figure 5:** Case C: Problem description with mesh (left) and deflection at the tip over time compared with results from [13] (right). Units in m.

The acceleration achieved with the presented models describes the same tendency as in Case A. Nevertheless, both methods reduce the required computational time in greater magnitude than before. The same case was reproduced by [7], showing similar levels of speed-up between block-coupled and segregated methods. In that case, a finite element software was tested too, and the block-coupled approach demonstrated fewer requirements in time (less than one third) and memory (less than half) for all meshes.

**Table 1:** Execution time and speed-up in all cases for each numerical approach: segregated (SA), segregated with convergence acceleration (SB) and block-coupled (C). The simulations have been carried out using 1 CPU core (3.4 GHz Intel Haswell processors).

	Case A				Case B				Case C			
	1	2	3	4	1	2	3	4	1	2	3	4
SA [s]	0.10	0.60	4.8	38	0.27	2.0	18	168	3615	3773	3958	356
SB [s]	0.09	0.31	2.5	25	0.17	1.0	4.9	39	1408	1112	2871	65
C [s]	0.07	0.15	1.0	10	0.06	0.17	1.1	11	302	274	221	4.0
SA/SB	1.1	1.9	1.9	1.5	1.6	2.1	3.8	4.3	2.6	3.4	1.4	5.4
SB/C	1.4	2.0	2.4	2.4	2.6	5.7	4.3	3.4	4.7	4.1	13	16

### 4.3 Case C: Vibration of a cantilever structure

In order to verify the time integration scheme and highlight the differences in computing efficiency among the models facing transient cases, the vibration of a cantilever 3D beam is studied. The case follows an example of [13], and is outlined in Fig. 5. Density is  $2600 \text{ kg/m}^3$ , Young's modulus  $10 \text{ MPa}$  and Poisson's ratio  $0.3$ . The force in  $y$  direction is increased linearly from zero to  $F = -500 \text{ N}$  during the first 7 seconds, and then it is released.

Unlike in the previous cases, here a unique mesh of  $80 \times 8 \times 8$  (see Fig. 5) has been

tested. The variations within the case comprise different time steps, i.e.  $\Delta t = 0.25$  s (1),  $\Delta t = 0.5$  s (2) and  $\Delta t = 1$  s (3), and a static simulation with a steady force of  $F = -500$  N (4).

The resulted transient response of the structure matches very well the solution from [13], as observed in Fig. 5. Time dedicated to conducting the whole transient and static simulations is summarised in Table 1. Being a bending case, strong coupling among displacement components arises, and greater speed-ups of the block-coupled model are achieved. The major benefit is obtained with the static case since transient cases alleviate these dependencies and allow starting the resolution of an instant with the time preceding solution as an initial guess, which is close to the new solution. Thus, the speed-up of the block-coupled method compared with the segregated method is lower for the shorter time steps. Potential improvements in the transient solver, such as a predictor step to extrapolate the value at the start of a time step may further reduce these differences between both approaches.

## 5 CONCLUSIONS

Two enhanced unstructured finite volume models for 3D linear thermoelastic materials have been presented. They both discretise the displacement in the cell centre and its gradient and stress directly on the cell faces. The first approach follows the traditional segregated method to solve the coupled linear system, but with the addition of a convergence acceleration technique. The second is based on a block-coupled method, which includes all the displacement inter-component relations within a unique system. After simulating three different cases, the proposed segregated model has shown great robustness and speed-ups between 1.1 and 5.4 as a result of the acceleration step. The block-coupled method has been able to predict the same results but with significantly less execution time: between 6 and 70 % of the time spent by the accelerated segregated method. However, higher memory usage and fine tuning of the linear solver to ensure convergence has been required.

## ACKNOWLEDGEMENTS

This work has been financially supported by the Ministerio de Educación, Cultura y Deporte, Spain (FPU13 fellowships), and by Ministerio de Economía, Industria y Competitividad, Spain (ENE2017-88697-R). Ignacio González would like to express his great appreciation to UCD School of Mechanical & Materials Engineering, particularly Professor Alojz Ivanković and Dr. Philip Cardiff, for their valuable help to implement advanced finite volume methods for structures during the short stay in their group.

## REFERENCES

- [1] I. Demirdžić and S. Muzaferija. Finite volume method for stress analysis in complex domains. *International Journal for Numerical Methods in Engineering*, 37(21):3751–3766, 1994.

- [2] H. Jasak and H. G. Weller. Application of the finite volume method and unstructured meshes to linear elasticity. *International Journal for Numerical Methods in Engineering*, 48(2):267–287, 2000.
- [3] D. Carolan, Ž. Tuković, N. Murphy, and A. Ivanković. Arbitrary crack propagation in multi-phase materials using the finite volume method. *Computational Materials Science*, 69:153–159, 2013.
- [4] P. Cardiff, Ž. Tuković, P. De Jaeger, M. Clancy, and A. Ivanković. A lagrangian cell-centred finite volume method for metal forming simulation. *International Journal for Numerical Methods in Engineering*, 109(13):1777–1803, 2017.
- [5] I. Demirdžić, S. Muzaferija, and M. Perić. Benchmark solutions of some structural analysis problems using the finite-volume method and multigrid acceleration. *International Journal for Numerical Methods in Engineering*, 40(10):1893–1908, 1997.
- [6] S. Das, S. R. Mathur, and J. Y. Murthy. An unstructured finite-volume method for structure–electrostatics interactions in mems. *Numerical Heat Transfer, Part B: Fundamentals*, 60(6):425–451, 2011.
- [7] P. Cardiff, Ž. Tuković, H. Jasak, and A. Ivanković. A block-coupled finite volume methodology for linear elasticity and unstructured meshes. *Computers & Structures*, 175:100–122, 2016.
- [8] A. Naseri, O. Lehmkuhl, I. González, and A. Oliva. Partitioned semi-implicit methods for simulation of biomechanical fluid-structure interaction problems. *Journal of Physics: Conference Series*, 745(3):032020, 2016.
- [9] I. González, A. Naseri, J. Rigola, C. D. Pérez-Segarra, and A. Oliva. A fluid-structure interaction solver for the fluid flow through reed type valves. *IOP Conference Series: Materials Science and Engineering*, 232(1):012032, 2017.
- [10] A. Naseri, O. Lehmkuhl, I. Gonzalez, E. Bartrons, C. D. Pérez-Segarra, and A. Oliva. A semi-implicit coupling technique for fluid–structure interaction problems with strong added-mass effect. *Journal of Fluids and Structures*, 80:94–112, 2018.
- [11] R. B. Hetnarski and M. R. Eslami. *Thermal Stresses - Advanced Theory and Applications*. Springer, 2009.
- [12] K. J. Bathe. *Finite Element Procedures*. Prentice Hall, 1996.
- [13] A. K. Slone, C. Bailey, and M. Cross. Dynamic solid mechanics using finite volume methods. *Applied Mathematical Modelling*, 27(2):69–87, 2003.
- [14] Ž. Tuković and H. Jasak. A moving mesh finite volume interface tracking method for surface tension dominated interfacial fluid flow. *Computers & Fluids*, 55:70–84, 2012.

- [15] P. Chandrashekar and A. Garg. Vertex-centroid finite volume scheme on tetrahedral grids for conservation laws. *Computers & Mathematics with Applications*, 65(1):58–74, 2013.
- [16] A. J. Macleod. Acceleration of vector sequences by multidimensional  $\Delta^2$  methods. *Communications in Applied Numerical Methods*, 2(4):385–392, 1986.
- [17] S. Balay, S. A., M. F. Adams, J. Brown, P. Brune, K. Buschelman, L. Dalcin, V. Eijkhout, W. D. Gropp, D. Kaushik, M. G. Knepley, L. C. McInnes, K. Rupp, B. F. Smith, S. Zampini, H. Zhang, and H. Zhang. PETSc users manual. Technical Report ANL-95/11 - Revision 3.8, Argonne National Laboratory, 2017.
- [18] S. Balay, W. D. Gropp, L. C. McInnes, and B. F. Smith. Efficient management of parallelism in object oriented numerical software libraries. In E. Arge, A. M. Bruaset, and H. P. Langtangen, editors, *Modern Software Tools in Scientific Computing*, pages 163–202. Birkhäuser Press, 1997.
- [19] National Agency for Finite Element Methods & Standards (Great Britain). *The standard NAFEMS benchmarks*. NAFEMS, 1990.